



The effects of beam drifts on elastic scattering measured by the large solid-angle covered detector array

Yong-Jin Yao^{1,2,3} · Cheng-Jian Lin³ · Lei Yang³ · Nan-Ru Ma³ ·
Dong-Xi Wang³ · Gao-Long Zhang² · Guang-Xin Zhang² · Hui-Ming Jia³ ·
Feng Yang³

Received: 18 November 2020 / Revised: 13 December 2020 / Accepted: 20 December 2020 / Published online: 15 February 2021
© China Science Publishing & Media Ltd. (Science Press), Shanghai Institute of Applied Physics, the Chinese Academy of Sciences, Chinese Nuclear Society 2021

Abstract A new detector array characterized by compact structure and large solid-angle coverage was designed for radioactive ion beam (RIB) experiments and measuring multi-particle correlations. A Monte Carlo simulation was performed to explore the effects of beam drifts in different directions and distances on the angular distribution of the Rutherford scattering, as measured by the detector array. The results indicate that when the beam drift distance is less than 2.0 mm, the symmetry of the detector array can maintain a count error of less than 5%. This confirms the property of the detector array for RIB experiments. Furthermore, the simulation was validated through the elastic scattering angular distributions of ${}^{6,7}\text{Li}$ measured by the detector array in ${}^{6,7}\text{Li} + {}^{209}\text{Bi}$ experiments at different energies.

Keywords Large solid-angle detector array · Beam drift · Monte Carlo simulation · Elastic scattering

1 Introduction

With the development of accelerator facilities in many nuclear physics laboratories, the beams of weakly bound nuclei are becoming increasingly available [1]. It is becoming critically important to understand the influence of weak binding on reaction dynamics, including elastic scattering [2–5]. Through the elastic scattering angular distributions of the weakly bound nuclei, reaction mechanisms can be studied [6, 7]. Therefore, a precise measurement of the elastic scattering angular distribution is necessary for the study of weakly bound nuclei.

A double-sided silicon strip detector (DSSD) is widely used for the measurement of charged particles because of its high position, energy resolution, and detection efficiency. Several well-known silicon detector arrays, such as the EXPADES detector array, MITA, and compact disk DSSD array [8–10], have been used for the measurement of elastic scattering angular distributions in experimental studies. A silicon detector array with a larger angle coverage than the previous arrays [8–15], both in scattering angles and azimuthal angles, was developed by the China Institute of Atomic Energy (CIAE). The detector array was characterized by a compact structure and small size. It contained eight independent telescopes, each of which consisted of two parts of silicon detectors: The first layer was 40 (or about 60) μm DSSD, followed by one or two layers of quadrant silicon detectors (QSDs) with different thicknesses. The detector array was used in the experiment of ${}^{6,7}\text{Li} + {}^{209}\text{Bi}$ at the HI-13 tandem accelerator in CIAE to

This work was supported by the National Natural Science Foundation of China (Nos. 11635015, U1832130, and 11975040), the State Key Laboratory of Software Development Environment (SKLSDE-2020ZX-16), the Continuous Basic Scientific Research Project (No. WDJC-2019-13), and the Leading Innovation Project (Nos. LC192209000701 and LC202309000201).

✉ Cheng-Jian Lin
cjlin@ciae.ac.cn

✉ Gao-Long Zhang
zgl@buaa.edu.cn

¹ State Key Laboratory of Software Development Environment, Beihang University, Beijing 100191, China

² School of Physics, Beihang University, Beijing 100191, China

³ China Institute of Atomic Energy, Beijing 102413, China

obtain the elastic scattering angular distributions of ${}^{6,7}\text{Li}$ at different energies. However, the elastic scattering angular distributions measured by the array were sensitive to the position of the beam spot on the target, while beam drifts were common in the experiments. In this study, we conducted Monte Carlo simulations to explore the effect of beam drifts on the angular distribution of Rutherford scattering. Through this method, we obtained precise angular distributions, which are in agreement with the calculated results.

In this paper, the detector array is described in Section II. The experimental setup is presented in Sect. III. In Sect. IV, we describe the Monte Carlo simulation method. In Sect. V, the scattered events of ${}^{6,7}\text{Li} + {}^{209}\text{Bi}$ are selected to obtain the elastic scattering angular distributions. Finally, we provide our conclusions.

2 Description of the detector array

The detector array used in the experiment is shown in Fig. 1. The detector array should have consisted of ten detector telescopes; however, two telescopes were canceled due to the lack of a silicon detector with the appropriate thickness. Each telescopic unit contained one DSSD and one (or two) QSDs. A mylar foil with a thickness of $0.5\ \mu\text{m}$ was installed in front of the telescope to protect the first silicon detector from being hit by a low-energy electron. Following the foil, a series of silicon detectors were aligned in the same plane. Different units had different arrangements. A DSSD with a thickness of about $40\ \mu\text{m}$ and a QSD with a thickness of $1000\ \mu\text{m}$ were arranged in

units 1, 2, 3, and 4. In units 5, 7, and 8, in case the energy loss of light particles in first layer of telescope was insufficient, a DSSD with a thickness of about $60\ \mu\text{m}$ and a QSD with a thickness of $300\ \mu\text{m}$, followed by a QSD with a thickness of $1000\ \mu\text{m}$, were arranged. Due to the lack of $300\ \mu\text{m}$ thick QSD, a DSSD with a thickness of about $60\ \mu\text{m}$ and a QSD with a thickness of $1500\ \mu\text{m}$ were arranged in unit 6. The gap between the mylar foil and DSSD was $1\ \text{mm}$, and the distance from the DSSD to the first QSD was about $4\ \text{mm}$.

The DSSDs were divided into 16 strips for each side, which had $50 \times 50\ \text{mm}^2$ total active area, making up 256 pixels of $3 \times 3\ \text{mm}^2$. The size of each pixel determines the angular resolution of the detector array. Considering the distance from the target to the DSSDs, which was about $70\ \text{mm}$ (or $82\ \text{mm}$), the angular resolution in the center region of each unit was at least about $\pm 1.23^\circ$ (or $\pm 1.05^\circ$), which became better in the periphery area of the detector telescopes in the laboratory frame. The QSDs were divided into four squares, and each square had a $24 \times 24\ \text{mm}^2$ active area.

The eight ΔE - E telescopes surrounding the target were installed on a designed and fixed frame. In the array, the distance from the center of the DSSD to the target center was $70\ \text{mm}$ in units 1, 2, 3, 4, 7, and 8, and $82\ \text{mm}$ in units 5 and 6. The angle of the center of each unit in the beam direction, which is marked as θ , is listed in Table 1. Another angle, ϕ , which is listed in Table 1, is the angle of the center of each unit in the vertical plane. The arrangement of eight telescopes made the array cover a large area, both for the scattering angle and azimuthal angle. The angular coverage of each unit is shown in Fig. 2.

To reduce the noise, the integrated preamplifiers designed in CIAE [16] were installed close to the detectors, so that the integrated preamplifiers were also arranged in the reaction chamber, which was evacuated in the experiment. A cooling system was used to decrease the temperature, to ensure that the integrated preamplifiers functioned stably. All integrated preamplifiers were installed on two hollow brass disks, which were fixed on the top and bottom of the array. During the experiment, the integrated preamplifiers transferred their heat to the disks, and the brass disks were cooled by the circulation of alcohol inside.

3 Experimental setup

The detector array was used to study the reaction mechanism in the ${}^{6,7}\text{Li} + {}^{209}\text{Bi}$ systems at energies around and above the Coulomb barrier. In the experiment, the ${}^{6,7}\text{Li}$ beams were accelerated to energies of 30, 40, and 47

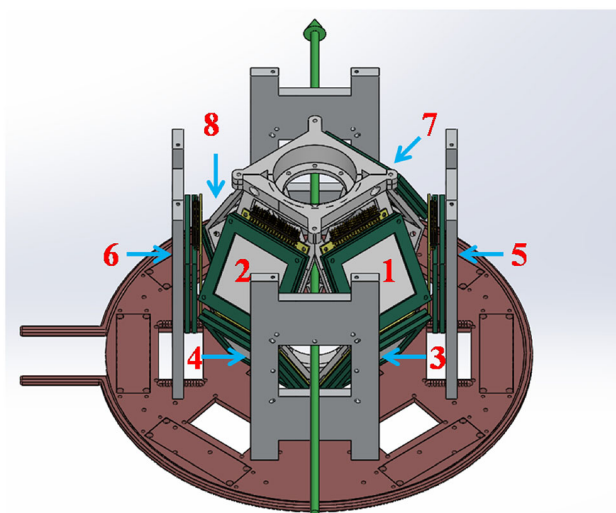


Fig. 1 (Color online) Setup of silicon detector array. To see the telescope units, the brass disk on the top is invisible. The rectangle sign on the disk is where the integrated preamplifiers were installed, and the left outstretched part is the input and output of the alcohol

Table 1 Brief information on the detector array

Unit NO.	Thickness of DSSD (μm)	Thickness of front QSD (μm)	Thickness of back QSD (μm)	Distance between unit and target (mm)	θ ($^\circ$)	ϕ ($^\circ$)
1	40	1000	***	70	132.07	139.23
2	40	1000	***	70	132.07	40.77
3	40	1000	***	70	132.07	220.77
4	40	1000	***	70	132.07	319.23
5	60	300	1000	82	90	180
6	60	1500	***	82	90	0
7	60	300	1000	70	47.93	139.23
8	60	300	1000	70	47.93	319.23

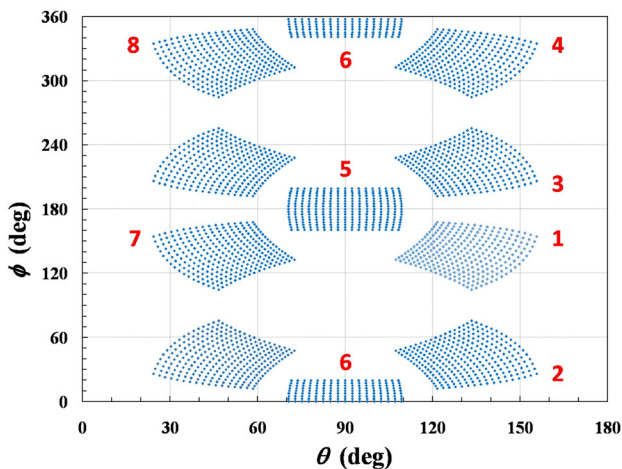


Fig. 2 (Color online) Angular coverage of detector array. Units 1–8 were used in the ${}^6\text{Li} + {}^{209}\text{Bi}$ experiment, and the other two telescopes were canceled. The array covers the scattering angle θ from 24.31° to 155.69° , and 300.96° in the azimuthal angle ϕ . Pixel separation in each detector is exaggerated for clarity

MeV, while the ${}^6\text{Li} + {}^{209}\text{Bi}$ experiment was performed at an energy of 25 MeV. The schematic vertical view of the experimental setup for ${}^6\text{Li} + {}^{209}\text{Bi}$ is shown in Fig. 3. The self-hold target ${}^{209}\text{Bi}$ with a thickness of $210 \mu\text{g}/\text{cm}^2$ was

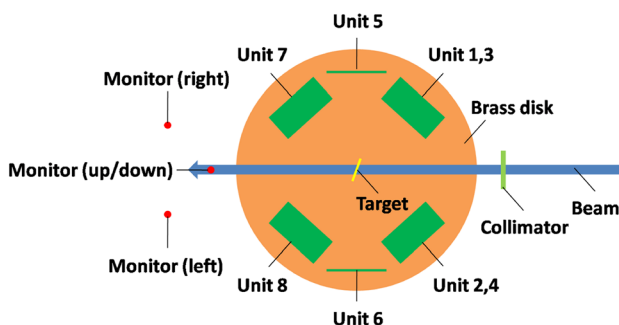


Fig. 3 (Color online) Schematic plot of the experimental setup viewed from a top-down perspective. The beam enters from the right side of the figure

located at the center of the detector array. To reduce the blind area on the detectors caused by the target frame, the target was tilted at 70° relative to the beam line, and aligned to the gap of the units. A collimator with a diameter of 3 mm was installed at 30 cm in front of the target along the beam line to limit the beam spot size and position. Four silicon detectors were installed at a distance of 250 mm from the center of the target to monitor the beam intensity and beam drifts. Two monitors with a diameter of 0.5 mm were installed symmetrically at a scattering angle of 12.5° in the horizontal plane, while the other two monitors with a radius of 0.5 mm were installed at a scattering angle of 25° in the vertical plane.

4 Simulation

It is common knowledge that the different reaction positions of the projectiles on the target represent different scattering angles for the particles measured by the same detector pixel. The beam spot size of the radioactive ion beam on the target was usually large (about 10 mm), which affected the accuracy of the scattering angle of the particles measured in the experiments. Therefore, several position-sensitive detectors, such as parallel plate avalanche counters, were often placed in front of the target to reconstruct the trajectories of beam particles and determine the reaction positions. For the beam generated by the HI-13 tandem accelerator, the beam spot size on the target was sufficiently small (at most 1 mm), so that the scattering angle of each particle could be directly obtained from the geometry relationship between the fired silicon pixel and beam spot.

However, beam drifts, leading to changes in the reaction positions of the beam particles on the target, were common in the experiments, and the accuracy of the scattering angle of the particles measured in the experiments was often affected. To determine the influence of beam drifts on the measurement via the detector array, a Monte Carlo

simulation was performed to simulate the angular distribution of the Rutherford scattering measured by the array [17]. In the simulation, the aforementioned geometry of the detector array including the eight telescopic units, was implemented, and the number of simulated events was 10^8 . The beam particles were simulated with the energies sampled from a Gaussian distribution with a large width to cover a wide range of energies. The distribution was centered (mean) at 25 MeV with an energy spread (σ) of 1 MeV. The ion distribution was uniform in circles with a radius of 0.5 mm, which was consistent with the beam spot size in the ${}^6,7\text{Li} + {}^{209}\text{Bi}$ experiments. The elastic scattering occurred inside the target with the reaction positions sampled from a random distribution along the beam line, and the energy loss of the projectiles in the target was taken into consideration by the calculation with the distances ${}^6\text{Li}$ traversed in the target.

The different beam drift distances in the horizontal and vertical directions were both chosen in the simulation. We used the ratios of the number of detected particles with different beam drift distances to those with no beam drift in the same pixels. By comparing the changes of ratios, the influence of beam drifts was obtained. To distinguish the directions of beam drifts, the distance was recorded as a positive value when the beam drifted to the right or down relative to the beam direction. The simulation results with different drift distances in the horizontal direction are shown in Fig. 4, while the results for beam drifts in the vertical direction are shown in Fig. 5. To distinguish easily, the scattering angles were partitioned into 4° bins. By comparing Figs. 4 and 5, it was easy to observe that the

ratios were closer to 1 when all detectors were cooperating. As shown in Fig. 4c, d, when the beam drifted in the horizontal direction, the ratios were lower than 1.05 when the beam drift distance was larger than -2 mm, and higher than 0.95 when the distance was less than 3 mm. When the beam drifted in the vertical direction, as shown in Fig. 5c, d, the difference between the ratios and standard value (the dashed line) was less than 4% when the beam drift distance ranges from -5 mm to 5 mm. This indicates that the beam drifts in the horizontal direction had a greater effect on the measured elastic scattering angular distribution than those in the vertical direction. This may result from the tilted target and the asymmetry of the detectors in the horizontal-vertical direction.

We concluded that the symmetrical placement of detector telescopes is beneficial for correcting the effect of beam drifts. The influence of beam drifts was small at distances from -2 mm to 4 mm in the horizontal direction or from -5 mm to 5 mm in the vertical direction, and the count error was less than 5%. When the beam drift distance was less than 1 mm, the influence was at most 2%.

5 Data analysis and results

To verify the above simulation, the elastic scattering data of ${}^6,7\text{Li} + {}^{209}\text{Bi}$, measured by the detector array, were analyzed. The energy calibrations of the DSSDs were performed utilizing the α particles decayed from the evaporation residues in both complete and incomplete fusion. In addition, two radioactive sources (${}^{239}\text{Pu}$ and

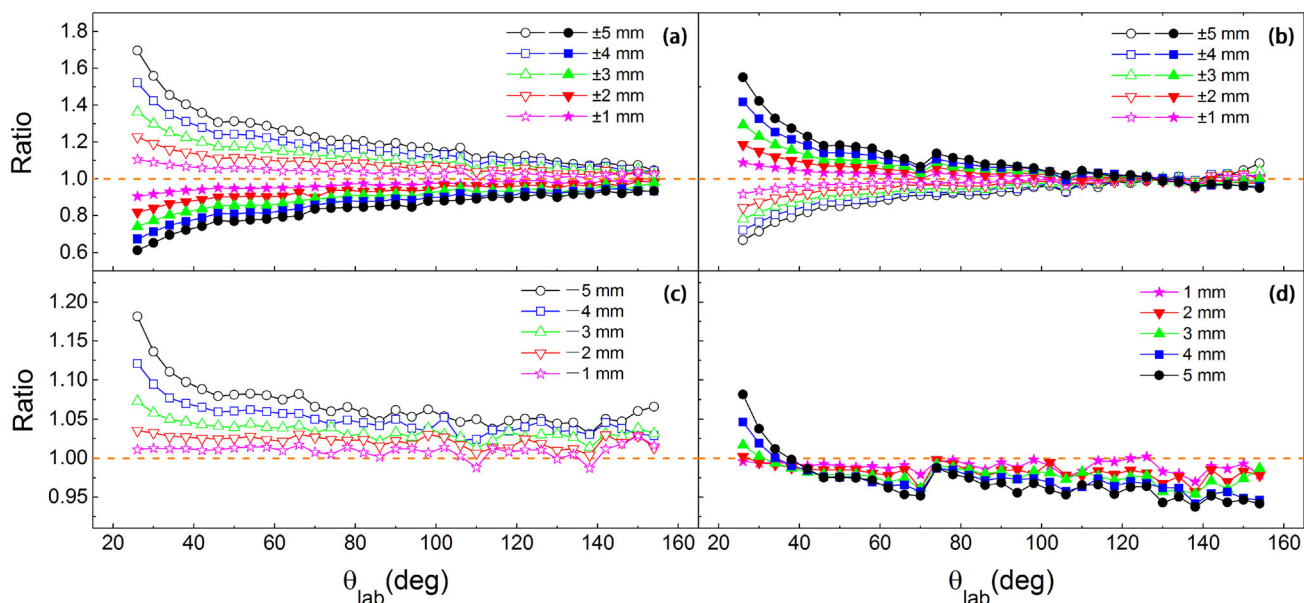


Fig. 4 (Color online) The ratios with beam drifts at different distances in the horizontal direction. **a, b** Results with the units to the right and left of the beam, respectively; **c, d** results with all units considering the symmetries of the array

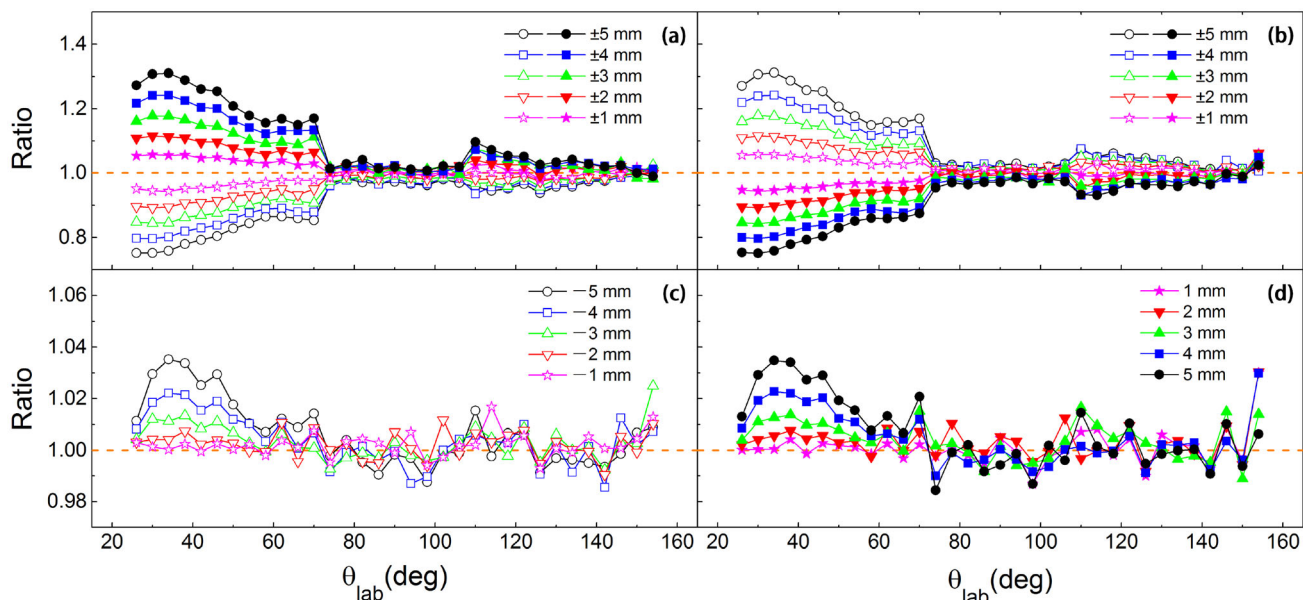


Fig. 5 (Color online) Ratios with beam drifts at different distances in the vertical direction. **a, b** results with the units above and below the beam, respectively; **c, d** results with all units considering the symmetries of the array

²⁴¹Am), providing α particles at energies of 5.156 MeV and 5.486 MeV, were employed to calibrate the energy spectrum. Then, the calibrations of the QSDs were performed by the energy deposited by charged particles in the QSDs, which were determined by subtracting the energy measured by the DSSDs from the expected energy of the particles calculated by LISE++ [18].

The typical particle identification spectrum in ⁶Li + ²⁰⁹Bi, which was obtained from one pixel of the unit 5 telescope at an energy of 40 MeV, is shown in Fig. 6a, and the spectra measured by unit 4 at the same scattering angle are shown in Fig. 6b, c. As labeled correspondingly, the banana-like regions in Fig. 6a–c can be identified as ⁶Li, protons, deuterons, tritons, and alphas.

A typical energy spectrum of ⁶Li + ²⁰⁹Bi, which was measured by unit 4 at an energy of 40 MeV, is shown in Fig. 7. The energy resolution was about 2.0%, which was sufficient to allow a clear separation between the elastic and inelastic scattering events (the first excited state energy of ⁶Li is 2186 keV). Then, the pure elastic scattering events of ⁶Li were chosen to calculate the elastic scattering angular distribution. This is the same for ⁷Li + ²⁰⁹Bi. Through the ratios of the elastic scattering events measured by the symmetrical monitors over a period of time, the average beam drift distance was obtained via calculation using the program, Mathematica [19]. Owing to the installed collimator, the beam drifts over the period of time were limited. Then, the influence of beam drifts was corrected via simulations using the determined beam drift distance.

The angular distribution of elastic scattering is usually described as the ratio of the reaction cross section to the cross section of the Rutherford scattering, which is obtained using equation [11]

$$\frac{d\sigma(\theta_C)}{d\sigma_{RU}(\theta_C)} = D \frac{N(\theta_C)}{N_{RU}(\theta_C)}, \tag{1}$$

where parameter D is a normalization constant that can be calculated by assuming that the elastic scattering is pure Rutherford scattering at small scattering angles. Subscript C refers to the center-of-mass frame. $N(\theta_C)$ is the elastic scattering event at any scattering angle, and $N_{RU}(\theta_C)$ is the Rutherford scattering event with the same solid angles at the same scattering angle in the center-of-mass frame.

We supposed the elastic scattering in ⁶Li + ²⁰⁹Bi at an energy of 25 MeV is pure Rutherford scattering because 25 MeV is below the Coulomb barrier of this system. Therefore, in the ⁶Li + ²⁰⁹Bi system, $N(\theta_C)$ is the elastic scattering count measured in the experiment at designed energies, and $N_{RU}(\theta_C)$ is the experimental elastic scattering count of ⁶Li + ²⁰⁹Bi at 25 MeV. Then, the equation becomes

$$\frac{d\sigma_{6Li}(\theta_C)}{d\sigma_{6Li,RU}(\theta_C)} = D_1 \frac{N_{6Li}(\theta_L)}{N_{6Li,25MeV}(\theta_L)}, \tag{2}$$

where θ_L is the scattering angle of ⁶Li in the laboratory frame, which corresponds to θ_C in the center-of-mass frame, while D_1 is the new normalization constant. The influence of the detector efficiency and geometry of the detector array was reduced by taking the elastic scattering

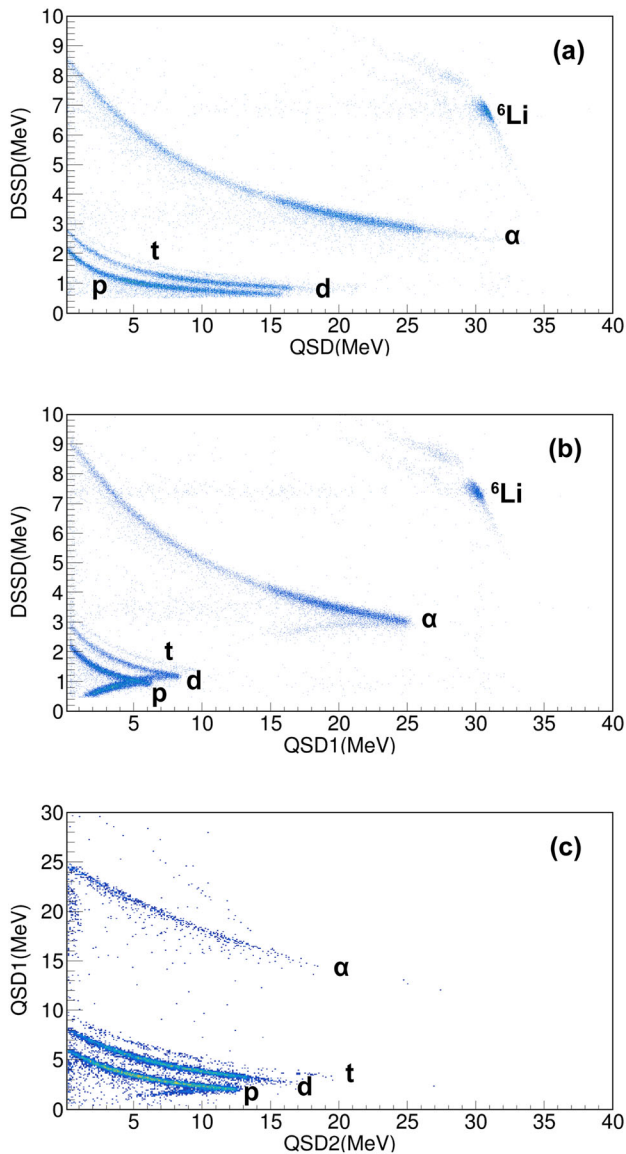


Fig. 6 (Color online) Typical spectra of ${}^6\text{Li} + {}^{209}\text{Bi}$ measured at $E_{\text{Lab}} = 40$ MeV and $\theta_{\text{Lab}} = 89^\circ$. **a** Measured by the telescope composed of DSSD and QSD in unit 5; **b** measured by the telescope composed of DSSD and front QSD in unit 4; **c** measured by the telescope composed of front QSD and back QSD in unit 4

in ${}^6\text{Li} + {}^{209}\text{Bi}$ at an energy of 25 MeV into calculations as Rutherford scattering.

For the calculation of the angular distributions of elastic scattering in the ${}^7\text{Li} + {}^{209}\text{Bi}$ system at different energies, a derivation is required. The number of Rutherford scattering events can be deduced from the elastic scattering events in ${}^6\text{Li} + {}^{209}\text{Bi}$ at an energy of 25 MeV, and the transformation equation is as follows:

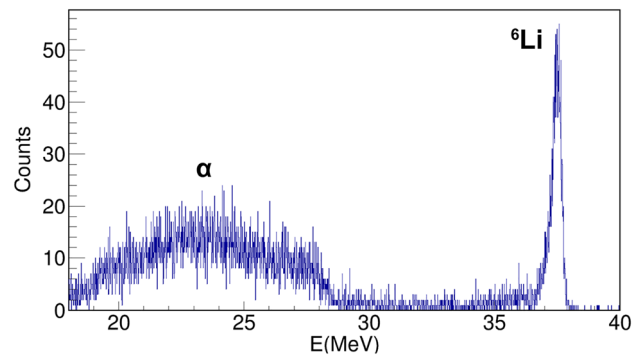


Fig. 7 (Color online) Typical energy spectrum of ${}^6\text{Li} + {}^{209}\text{Bi}$ at $E_{\text{Lab}} = 40$ MeV and $\theta_{\text{Lab}} = 89^\circ$

$$N_{7\text{Li,RU}}(\theta_{1,C}) = N_{6\text{Li,RU}}(\theta_C) \frac{\Omega_{7\text{Li,RU}}(\theta_{1,C})}{\Omega_{6\text{Li,RU}}(\theta_C)}, \tag{3}$$

$$\times \frac{d\sigma_{7\text{Li,RU}}(\theta_{1,C})}{d\Omega_{7\text{Li,RU}}(\theta_{1,C})} \frac{d\Omega_{6\text{Li,RU}}(\theta_C)}{d\sigma_{6\text{Li,RU}}(\theta_C)},$$

where θ_C and $\theta_{1,C}$ are the scattering angles of ${}^{6,7}\text{Li}$, respectively, in the center-of-mass frames. $\Omega_{7\text{Li,RU}}(\theta_{1,C})$ and $\Omega_{6\text{Li,RU}}(\theta_C)$ are the solid angles of ${}^{6,7}\text{Li}$ at the corresponding scattering angles. If θ_C and $\theta_{1,C}$ correspond to the same scattering angle θ_L in the frame of the laboratory system, the Rutherford scattering events of ${}^7\text{Li}$ at the scattering angle $\theta_{1,C}$ can be described as:

$$N_{7\text{Li,RU}}(\theta_{1,C}) = D_2 P N_{6\text{Li,RU}}(\theta_C)$$

$$\frac{\sin^4 \left(\left(\theta_L + \sin^{-1} \left(\frac{A_{6\text{Li}}}{A_{209\text{Bi}}} \sin \theta_L \right) \right) / 2 \right)}{\sin^4 \left(\left(\theta_L + \sin^{-1} \left(\frac{A_{7\text{Li}}}{A_{209\text{Bi}}} \sin \theta_L \right) \right) / 2 \right)}, \tag{4}$$

$$\frac{\left(1 + \left(\frac{A_{7\text{Li}}}{A_{209\text{Bi}}} \right)^2 + 2 \frac{A_{7\text{Li}}}{A_{209\text{Bi}}} \cos \left(\theta_L + \sin^{-1} \left(\frac{A_{7\text{Li}}}{A_{209\text{Bi}}} \sin \theta_L \right) \right) \right)^{3/2}}{1 + \frac{A_{7\text{Li}}}{A_{209\text{Bi}}} \cos \left(\theta_L + \sin^{-1} \left(\frac{A_{7\text{Li}}}{A_{209\text{Bi}}} \sin \theta_L \right) \right)}$$

$$P = \frac{\left(1 + \left(\frac{A_{6\text{Li}}}{A_{209\text{Bi}}} \right)^2 + 2 \frac{A_{6\text{Li}}}{A_{209\text{Bi}}} \cos \left(\theta_L + \sin^{-1} \left(\frac{A_{6\text{Li}}}{A_{209\text{Bi}}} \sin \theta_L \right) \right) \right)^{3/2}}{1 + \frac{A_{6\text{Li}}}{A_{209\text{Bi}}} \cos \left(\theta_L + \sin^{-1} \left(\frac{A_{6\text{Li}}}{A_{209\text{Bi}}} \sin \theta_L \right) \right)} \tag{5}$$

where D_2 is a constant related to the energies of ${}^{6,7}\text{Li}$, and P is the ratio of the solid angle of ${}^7\text{Li}$ to ${}^6\text{Li}$ in the center-of-mass frame at the same scattering angle θ_L . Then, the ratio to describe the angular distribution of elastic scattering of ${}^7\text{Li}$ with ${}^{209}\text{Bi}$ can be calculated by substituting Eq. (4) and Eq. (2) in Eq. (1).

$$\frac{d\sigma_{7\text{Li}}(\theta_{1,C})}{d\sigma_{7\text{Li,RU}}(\theta_{1,C})} = \frac{D_3}{P} \frac{N_{7\text{Li}}(\theta_L)}{N_{6\text{Li},25\text{MeV}}(\theta_L)} \times \frac{\sin^4\left(\left(\theta_L + \sin^{-1}\left(\frac{A_{7\text{Li}}}{A_{209\text{Bi}}}\sin\theta_L\right)\right)/2\right)}{\sin^4\left(\left(\theta_L + \sin^{-1}\left(\frac{A_{6\text{Li}}}{A_{209\text{Bi}}}\sin\theta_L\right)\right)/2\right)}, \tag{6}$$

where parameter D_3 is the normalization constant for ^7Li .

The normalization results of the elastic scattering for ^6Li on the ^{209}Bi target at energies of 30, 40, and 47 MeV are shown in Fig. 8a, while those for ^7Li at the same energies are shown in Fig. 8b. The results were fitted by the optical model calculation program ‘‘Ptolemy’’ [20], and the potential parameters and total reaction cross sections were extracted from the model. Here, the Woods–Saxon function was selected as the shape function of the real and imaginary parts of the nuclear potential. V , r_V , a_V , respectively, and W , r_W , and a_W , respectively, represent the amplitude, radius parameter, and diffuseness parameter of the real and imaginary parts of the nuclear potential. The fitting results are shown in Fig. 8 by the solid curves, and the potential parameters and the total reaction cross sections are listed in Table 2. In Fig. 8, we observed that the experimental data were fitted well at 30 MeV and 40 MeV, while the fit lines deviated the experimental data at large angles of 47 MeV, because the events measured at large angles of 47 MeV were too small and other reaction channels opened. Because the fitting results are in agreement with the experimental data, the results in Table 2

provide the reference data for the nuclear potential and total cross sections of $^{6,7}\text{Li} + ^{209}\text{Bi}$.

6 Summary

In this study, we conducted a study introducing the elastic scattering measured by a large solid-angle covered detector array, a silicon detector telescope array designed in CIAE, which covered the scattering angle from 24.31° to 155.69° and 300.96° in the azimuthal angle in the laboratory system. By simulating the angular distributions of Rutherford scattering measured by the detector array at different beam drift distances in the horizontal and vertical directions, we explored the influence of the beam drifts on the angular distribution of the Rutherford scattering measured by the detector array, obtaining the precise angular distribution of elastic scattering. The simulation results indicate that benefiting from the symmetrical geometry of the detector array, the count error was less than 2% when the beam drift distance was less than 1 mm. The beam drifts had a weak influence on the measurements with the array.

The elastic scattering angular distributions, measured by the detector array in the $^{6,7}\text{Li}$ experiments with the ^{209}Bi target at energies of 30, 40, and 47 MeV and performed at CIAE, were chosen to validate the simulation. After obtaining the elastic scattering angular distributions of $^{6,7}\text{Li}$, the optical model calculation program ‘‘Ptolemy’’ was used to fit the results at different energies. The

Fig. 8 (Color online) Angular distributions of elastic scattering of (a) ^6Li and (b) ^7Li on ^{209}Bi at $E_{\text{Lab}} = 30, 40, 47$ MeV. The solid circles represent the experimental data, and the solid curves show the fitting results obtained by the optical model. Error bars are statistical only

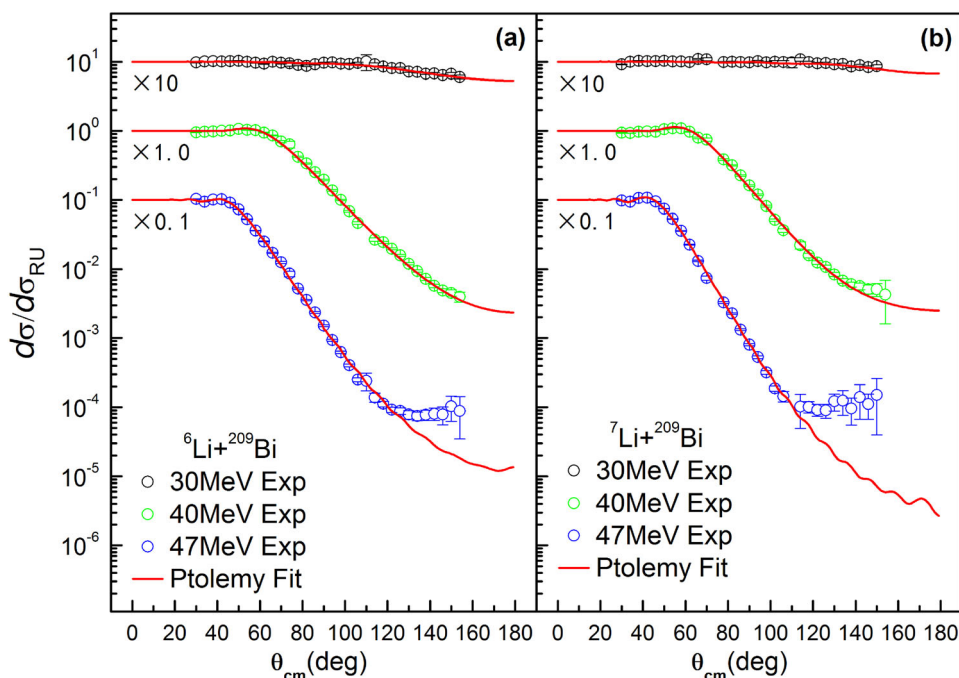


Table 2 Optical potential parameters and total reaction cross sections extracted from the ${}^6\text{Li} + {}^{209}\text{Bi}$ elastic scattering data

Projectile	E_{Lab} (MeV)	V (MeV)	r_V (fm)	a_V (fm)	W (MeV)	r_W (fm)	a_W (fm)	σ_R (mb)
${}^6\text{Li}$	30.0	13.61	1.33	0.36	24.18	0.26	2.00	284.46
	40.0	28.48	1.13	0.80	12.66	1.26	0.69	1062.20
	47.0	44.26	1.22	0.50	13.43	0.95	1.43	1840.63
${}^7\text{Li}$	30.0	6.72	1.39	0.40	22.09	0.49	1.54	114.44
	40.0	32.52	1.15	0.77	13.60	1.26	0.58	1011.11
	47.0	41.79	1.24	0.51	24.46	0.70	1.58	1855.36

program fitted the experimental data well. The potential parameters V , r_V , a_V , W , r_W , a_W , and total reaction cross sections were extracted from the fitting. The agreement between the experimental results and theoretical calculations and the previous results [21] verifies the accuracy of the simulation. Furthermore, the method can be used in ${}^8\text{B} + {}^{120}\text{Sn}$ and ${}^7\text{Be} + {}^{209}\text{Bi}$ experiments to confirm the performance of the detector array for a deeper investigation of the nuclear reaction mechanism.

Author Contributions All authors contributed to the study conception and design. Material preparation, data collection, and analysis were performed by Nan-Ru Ma, Dong-Xi Wang, and Yong-Jin Yao. The first draft of the manuscript was written by Yong-Jin Yao, and all authors commented on previous versions of the manuscript. All authors read and approved the final manuscript.

References

1. C. Signorini, A. Edifizi, M. Mazzocco et al., Exclusive breakup of ${}^6\text{Li}$ by ${}^{208}\text{Pb}$ at Coulomb barrier energies. *Phys. Rev. C* **67**, 044607 (2003). <https://doi.org/10.1103/PhysRevC.67.044607>
2. L.F. Canto, P.R.S. Gomes, R. Donangelo et al., Recent developments in fusion and direct reactions with weakly bound nuclei. *Phys. Rep.* **596**, 1–86 (2015). <https://doi.org/10.1016/j.physrep.2015.08.001>
3. N. Keeley, R. Raabe, N. Alamanos, J.L. Sida, Fusion and direct reactions of halo nuclei at energies around the Coulomb barrier. *Prog. Particle Nucl. Phys.* **59**, 579–630 (2007). <https://doi.org/10.1016/j.pnpnp.2007.02.002>
4. K.J. Cook, E.C. Simpson, L.T. Bezzina et al., Origins of Incomplete Fusion Products and the Suppression of Complete Fusion in Reactions of ${}^7\text{Li}$. *Phys. Rev. Lett.* **122**, 102501 (2019). <https://doi.org/10.1103/PhysRevLett.122.102501>
5. M. Dasgupta, P.R.S. Gomes, D.J. Hinde et al., Effect of breakup on the fusion of ${}^6\text{Li}$, ${}^7\text{Li}$ and ${}^9\text{Be}$ with heavy nuclei. *Phys. Rev. C* **70**, 024606 (2004). <https://doi.org/10.1103/PhysRevC.70.024606>
6. M. Mazzocco, D. Torresi, D. Pierroutsakou et al., Direct and compound-nucleus reaction mechanisms in the ${}^7\text{Be} + {}^{58}\text{Ni}$ system at near-barrier energies. *Phys. Rev. C* **92**, 024615 (2015). <https://doi.org/10.1103/PhysRevC.92.024615>
7. E.F. Aguilera et al., Near-Barrier Fusion of the ${}^8\text{B} + {}^{58}\text{Ni}$ Proton-Halo System. *Phys. Rev. Lett.* **107**, 092701 (2011). <https://doi.org/10.1103/PhysRevLett.107.092701>
8. E. Strano, A. Anastasio, M. Bettini et al., The high granularity and large solid angle detection array EXPADES. *Nucl. Instr. Methods Phys. Res. B* **317**, 657–660 (2013). <https://doi.org/10.1016/j.nimb.2013.06.035>
9. D. Pierroutsakou, A. Boiano, C. Boiano et al., The experimental setup of the RIB in-flight facility EXOTIC. *Nucl. Instr. Methods Phys. Res. A* **837**, 46–70 (2016). <https://doi.org/10.1016/j.nima.2016.07.019>
10. N.R. Ma et al., MITA: A Multilayer Ionization-chamber Telescope Array for low-energy reactions with exotic nuclei. *Eur. Phys. J. A* **55**, 87 (2019). <https://doi.org/10.1140/epja/i2019-12765-7>
11. G.L. Zhang, Y.J. Yao, G.X. Zhang et al., A detector setup for the measurement of angular distribution of heavy-ion elastic scattering with low energy on RIBLL. *Nucl. Sci. Tech.* **28**, 104 (2017). <https://doi.org/10.1007/s41365-017-0249-0>
12. K.J. Cook, E.C. Simpson, D.H. Luong et al., Importance of lifetime effects in breakup and suppression of complete fusion in reactions of weakly bound nuclei. *Phys. Rev. C* **93**, 064604 (2016). <https://doi.org/10.1103/PhysRevC.93.064604>
13. S. Kalkal, E.C. Simpson, D.H. Luong et al., Asymptotic and near-target direct breakup of ${}^6\text{Li}$ and ${}^7\text{Li}$. *Phys. Rev. C* **93**, 069904 (2016). <https://doi.org/10.1103/PhysRevC.93.069904>
14. D.H. Luong, M. Dasgupta, D.J. Hinde et al., Predominance of transfer in triggering breakup in sub-barrier reactions of ${}^{6,7}\text{Li}$ with ${}^{144}\text{Sm}$, ${}^{207,208}\text{Pb}$ and ${}^{209}\text{Bi}$. *Phys. Rev. C* **88**, 034609 (2013). <https://doi.org/10.1103/PhysRevC.88.034609>
15. D.H. Luong, M. Dasgupta, D.J. Hinde et al., Insights into the mechanisms and time-scales of breakup of ${}^{6,7}\text{Li}$. *Phys. Lett. B* **695**, 105–109 (2011). <https://doi.org/10.1016/j.physletb.2010.11.007>
16. D.X. Wang, C.J. Lin, L. Yang et al., Compact 16-channel integrated charge-sensitive preamplifier module for silicon strip detectors. *Nucl. Sci. Tech.* **31**, 48 (2020). <https://doi.org/10.1007/s41365-020-00755-0>
17. G.X. Zhang, G.L. Zhang, C.J. Lin et al., The calibration of elastic scattering angular distribution at low energies on HIRFL-RIBLL. *Nucl. Instr. Methods Phys. Res. A* **846**, 23–28 (2017). <https://doi.org/10.1016/j.nima.2016.11.058>
18. O.B. Tarasovab, D. Bazina, LISE++: design your own spectrometer. *Nucl. Phys. A* **746**, 411–414 (2004). <https://doi.org/10.1016/j.nuclphysa.2004.09.063>
19. J. Mocaka, A.M. Bond, Use of MATHEMATICA software for theoretical analysis of linear sweep voltammograms. *J. Electroanal. Chem.* **561**, 191–202 (2004). <https://doi.org/10.1016/j.jelechem.2003.08.004>
20. M. H. Macfarlane, S. C. PIEPER. PTOLEMY: A program for heavy-ion direction-reaction calculation [R]. US : Argonne National Laboratory (1978)
21. S. Santra, S. Kailas, K. Ramachandran et al., Reaction mechanisms involving weakly bound ${}^6\text{Li}$ and ${}^{209}\text{Bi}$ at energies near the Coulomb barrier. *Phys. Rev. C* **83**, 034616 (2011). <https://doi.org/10.1103/PhysRevC.83.034616>